Supplementary Information

Light-driven sp^3-sp^3 cross-coupling of carboxylic acids and alkyl halides over a Ni single-atom catalyst

Mark A. Bajada,[1] *Giovanni Di Liberto,*[2] *Sergio Tosoni,*[2,*] *Vincenzo Ruta,*[1] *Alessandra Sivo,*[1] *Gianfranco Pacchioni,*[2] *and Gianvito Vilé*[1,*]

[1] *Department of Chemistry, Materials, and Chemical Engineering "Giulio Natta", Politecnico di Milano, Piazza Leonardo da Vinci 32, 20133 Milano, Italy.*

[2] *Department of Materials Science, Università di Milano Bicocca, via R. Cozzi 55, 20125 Milano, Italy.*

* *Corresponding authors. E-mails: sergio.tosoni@unimib.it (Prof. Dr. Sergio Tosoni); gianvito.vile@polimi.it (Prof. Dr. Gianvito Vilé)*

Materials and methods

Material synthesis. All reagents for the synthetic part of the work were purchased from commercial suppliers and used directly without any further purification. $Ni_{SA}–nCN_x$ was prepared through a modified published procedure.[1,2] In brief, graphitic carbon nitride (gCN_x) was first prepared using dicyanamide as a source of carbon and nitrogen. In a typical experiment, dicyanamide (10 g) was placed in an alumina crucible and heated in air at 550 °C for 3 h, at a heating rate of 10 °C min^{-1}. To prepare the nanosheets, gCN_x (750 mg) was thinly spread out in the alumina combustion boat, making good contact with air, and then heated at 520 °C for 4.5 h, using a heating rate of 2 °C min^{-1}. A pale-yellow powdered material was obtained. The nanosheets of carbon nitride were used as such as a photoactive support for the dispersion of the nickel single atoms. Specifically, $Ni(NO_3)_2·6H_2O$ in (Millipore) water (140 mg, 14 mL) was added dropwise to nCN_x (350 mg) and the resultant suspension was sonicated for 30 min, and then left for 12 h under ambient conditions. Sodium borohydride ($NaBH_4$, 1.05 g) was dissolved in Millipore water (5 mL) and was added dropwise to the stirring suspension. The mixture was stirred for a further 12 h at 80 °C, followed by twenty runs (1 min each) of rapid microwave heating (LG, power 1000 W). The resultant solid was redispersed in Millipore water, filtered, washed with plenty of water and ethanol, and left to dry in the oven at 55 °C for 3 h. The final material was denoted as "$Ni_{SA}–nCN_x$", and its single site nature was confirmed through in-depth characterization, in accordance with the published findings.

Material characterization. Powder X-ray diffraction (XRD) patterns were collected on a PANalytical X'Pert PRO MPD diffractometer equipped with an X'Celerator detector and with iron-filtered Co Kα (40 kV, 30 mA, $\lambda = 0.1789$ nm) radiation. using a 0.01° s–1 (2θ) scanning speed. The angular range of measurement was set as $2\theta = 5°–60°$, with a step size of 0.01°. The Ni content was determined by ICP-MS on an Agilent 7700x (Agilent, Japan). A weighted amount of sample from the catalyst (0.01 mg) was digested in nitric acid using a microwave. Elemental C, N, and H analysis was accomplished by combustion using a Vario Micro device. High-resolution transmission electron microscopy (HRTEM) images were obtained over a Titan G2 60-300 microscope (FEI), equipped with an X-FEG-type emission gun operating at 300 kV. High-angle annular dark-field detector (HAADF) scanning transmission electron microscopy (STEM) analysis was conducted over a Titan G2 60-300 microscope (FEI), equipped with HAADF detector 3000 (Fishione). Nitrogen physisorption was performed on a Micromeritics

ASAP 3020 instrument (Micromeritics, Atlanta) at −196 °C. Before the measurement, the samples (ca. 20–40 mesh) were degassed at 150 °C for 24 h. The specific surface area was determined by the Brunauer–Emmett–Teller (BET) method using the adsorption branch in the p/p0 range of 0.05–0.35. X-ray photoelectron spectroscopy (XPS) measurements were carried out in a custom-designed UHV system working at the base pressure of 1×10^{-9} mbar and equipped with an electron analyzer (EA125 Omicron) and an X-ray source (DAR400 Omicron). The powder samples were suspended in methanol and drop-cast on metal support to obtain a homogeneous film. Once dried, the sample was introduced in an ultrahigh-vacuum system and left outgassing overnight. Photoemission spectra were acquired at room temperature in normal emission. The spectra were analyzed using the XPSPEAK software using Voigt functions and subtracting a Shirley background. X-ray absorption spectroscopy (XAS) at the Ni K edge was recorded at the SuperXAS beamline of the Swiss Light Source (Paul Scherrer Institut, Villigen, Switzerland). Measurements were performed ex situ in transmission mode on pellets, and a Ni foil was measured simultaneously for absolute energy calibration. The quick-EXAFS (QEXAFS) method was used to collect 100 spectra in 100 s, which were then merged. Athena of the Demeter software package was used for normalization and background subtraction. The fit of the EXAFS spectra was performed by using the NiO structure for the path description. The amplitude reduction factor was calculated from EXAFS fits of the Ni reference foil assuming a coordination number of 12.

Photocatalytic experiments. Ni_{SA}–nCN_x (5 mg), N-Boc proline (0.45 mmol, 1.5 equiv), K_2CO_3 (0.6 mmole, 2.0 equiv), H_2O (6 mmole, 20.0 equiv), solvent (3 mL), and a magnetic stirrer bar were transferred into a 4 mL vial equipped with a screw cap rubber septum, which in-turn functioned as the batch photoreactor. The reaction mixture was degassed by bubbling a N_2 stream for 15 min at 0 °C. Then, 1-bromo-3-phenylpropane (0.30 mmol, 1.0 equiv) was added dropwise into the solution. Photocatalytic batch experiments were carried out using a PhotoCube™ reactor (ThalesNano Inc.), and an irradiation time of 8 h (unless otherwise stated). The preliminary product analysis was conducted using NMR spectroscopy. Essentially, the reaction mixture was filtered through a PTFE syringe filter (0.45 µm) and concentrated in vacuo; ^{1}H and ^{13}C NMR spectroscopic analysis were performed on a Bruker DPX 400 spectrometer at 298 K. To quantify the conversion of the limiting reagent (i.e., the 1-bromo-3-phenylpropane) after the reaction, a 30 µL aliquot of the solution was taken from the batch photoreactor and

diluted with 2.97 mL of MeCN, filtered, and then analyzed via high-performance liquid chromatography (HPLC). Conversion of 1-bromo-3-phenylpropane was deduced using an Agilent 1200 instrument, with an ultraviolet-visible detector (G1315D) set at 210 nm. Samples and standards (5 µL) were injected directly onto a 250 mm × 4.6 mm Hypersil GOLD™ aQ 5 µm 175 Å column purchased from Thermo Scientific. The mobile phase was comprised of a 60/40 MeCN/H_2O mixture with a total flow rate of 0.7 mL min^{-1} at 40 °C. When conducting the analysis, one hour of equilibration was required before the first sample injection. Initially, 1-bromo-3-phenylpropane was analyzed in isolation, to identify the respective retention time on the chromatogram (N-Boc proline was not visible at the available detection wavelength). A standard calibration curve of 1-bromo-3-phenylpropane (*i.e.*, the limiting reagent) was produced (Supplementary Information, Fig. S7); this allowed for the concentration of alkyl halide in the reaction aliquot to be deduced, and hence, for the starting material conversion and reaction rate to be computed.

For experiments invoking the use of alternative catalytic systems, the same reaction vial (with 1-bromo-3-phenylpropane as the alkyl halide) was adopted, as previously described, but the following quantities of the homogeneous photocatalyst and/or homogeneous nickel catalyst (plus ligating agent) were employed: $Ir[dF(CF_3)ppy]_2(dtbbpy)PF_6$ (0.02 equiv), $NiCl_2$•glyme (0.1 equiv), 4,4´-di-methoxy-2,2´-bipyridyl (0.1 equiv), in accordance with the published procedure.[3]

For the recovery and reutilization of the catalyst, after completion of the reaction involving 1-bromo-3-phenylpropane, the mixture was first filtered through a Millipore filtration setup (using a 0.45 µm PTFE membrane filter). The recovered material was then rinsed under vacuum with water and acetone, and dried overnight at 45 °C.

Theoretical calculations. Density Functional Theory (DFT) calculations were performed with the VASP code.[3,4] H(1s), C(2s,2p), N(2s,2p), Br(4s,4p), and Ni(3d,4s) electrons were treated explicitly, and the interaction between the inner electrons and the nuclei was treated with the Projector Augmented Wave method.[5,6] The exchange-correlation functional proposed by Perdew, Burke, and Ernzerhof (PBE) was adopted.[7] In some cases (vide infra), single point calculations on top of PBE results were done with the hybrid functional HSE06 to improve the electronic structure description.[8,9] The long-range dispersion was added to the potential according to Grimme's

DFT+D3 scheme with a Becke-Johnson damping function.[10,11] Structure relaxations were performed at the Γ point with a cutoff of 400 eV recurring to a conjugated gradient algorithm. Spin-polarization effects were included in all calculations. Dipole and quadrupole corrections to the total energy were applied along the non-periodic direction for all calculations on slab models. A vacuum region of at least 1.5 nm was included along the non-periodic direction in the supercell, to avoid spurious interactions between a replica of the slab models. The carbon nitride nanosheets have been modelled assuming a corrugated heptazine structure.[12–14] Gibbs free energies profiles have been determined by adopting the computational approach pioneered by Nørskov and co-workers,[15,16] to study reactions involving gas-phase molecules,[17–21] where we added the standard entropies of gas species to the calculated DFT energies. The entropy of all gas species (H_2, Br_2, CO_2) involved in the reaction cycle have been taken from the literature.[22]

Table S1. Compositional and textural characterization of the gCN_x, nCN_x, and $Ni_{SA}–nCN_x$ samples.

	C[a] / wt.%	**N[a] / wt.%**	**H[a] / wt.%**	**C:N[a] / -**	**Ni[b] / wt.%**	**S_{BET}[c] / m^2 g^{-1}**
gCN_x	31.39	47.30	2.34	0.66	-	11.8
nCN_x	32.15	47.92	2.12	0.67	-	27.9
$Ni_{SA}–nCN_x$	32.46	48.16	2.38	0.67	7.4	29.7

[a] CHNS data; [b] ICP-OES data; [c] BET to the N_2 isotherm collected at 77 K.

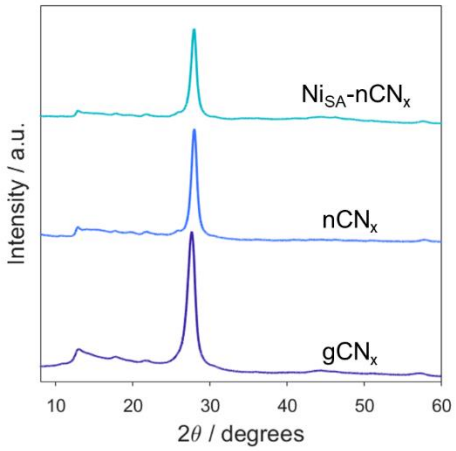

Fig. S1. Wide-angle X-ray diffraction patterns of gCN_x, nCN_x, and Ni_{SA}–nCN_x.

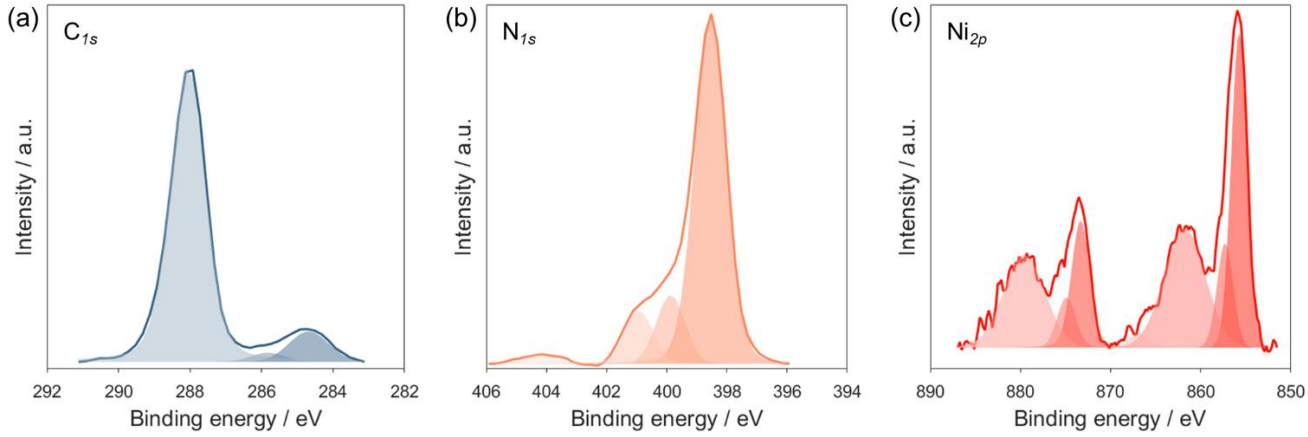

Fig. S2. High-resolution C 1*s*, N 1*s*, and Ni 2*p* X-ray photoelectron spectroscopy of Ni_{SA}–nCN_x.

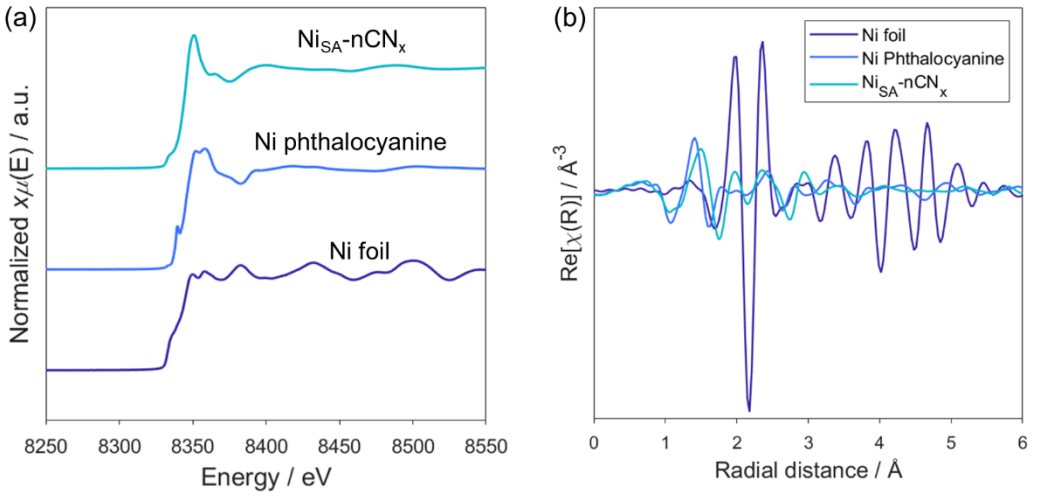

Fig. S3. X-ray absorption near edge structure (a) and its filtered fine structure (b) of a reference Ni foil, a reference Ni phthalocyanine homogeneous organocatalyst, and the Ni_{SA}–nCN_x catalyst.

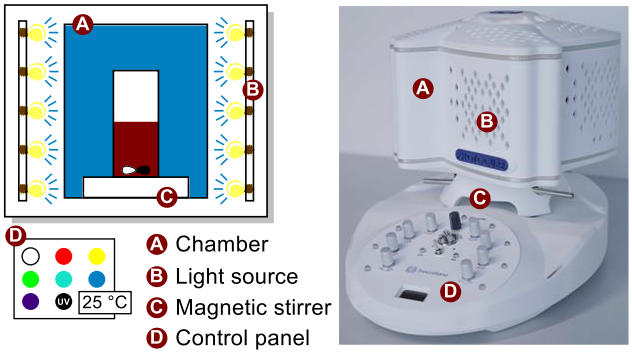

Fig. S4. Scheme and photograph of the ThalesNano PhotoCube™ reactor.

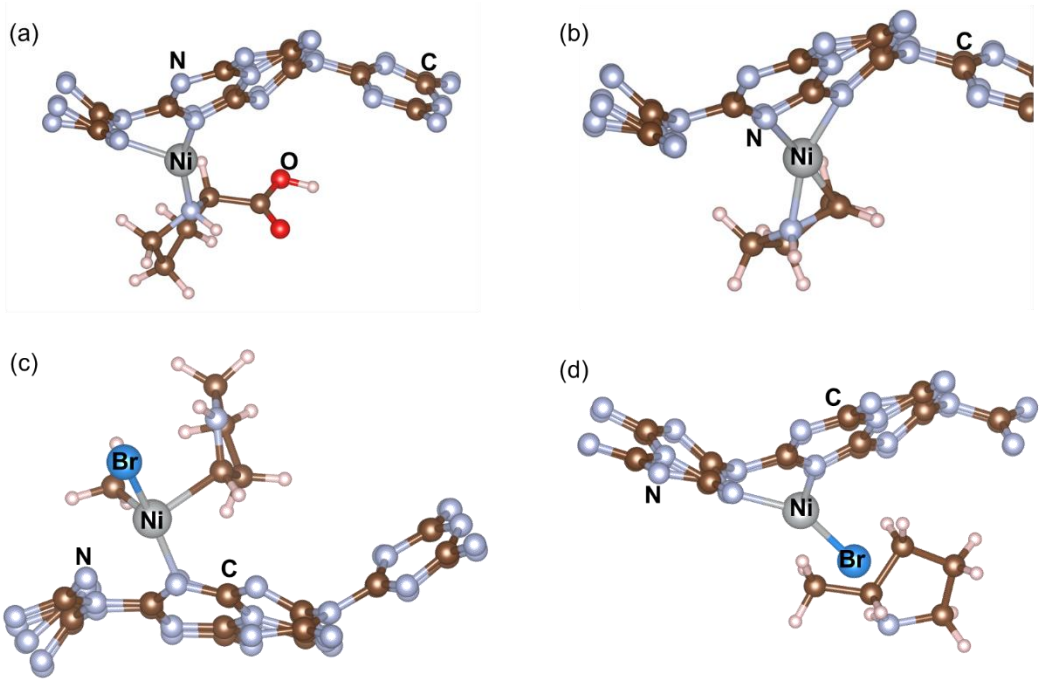

Fig. S5. Ball-and-stick models of the optimized molecular intermediates: (a) pyrrolidine-2-carboxylic acid on Ni_1–nCN_x; (b) pyrrolidine on Ni_1–nCN_x; (c) CH_3Br and pyrrolidine co-adsorbed on Ni_1–nCN_x; (d) Br bound to Ni and 2-methyl-pyrrolidine physisorbed on nCN_x.

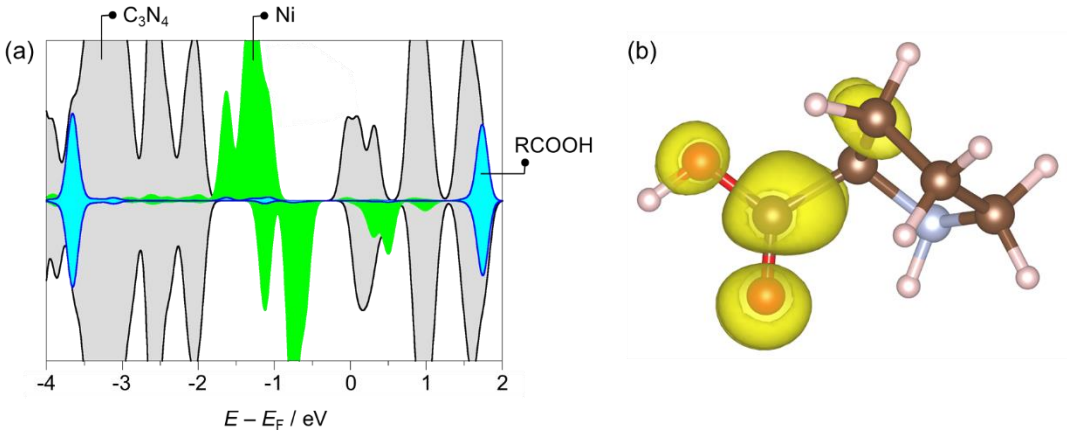

Fig. S6. (a) Projected Density of State for R-COOH on Ni–nCN_x, and (b) charge density plot of the R-COOH LUMO band.

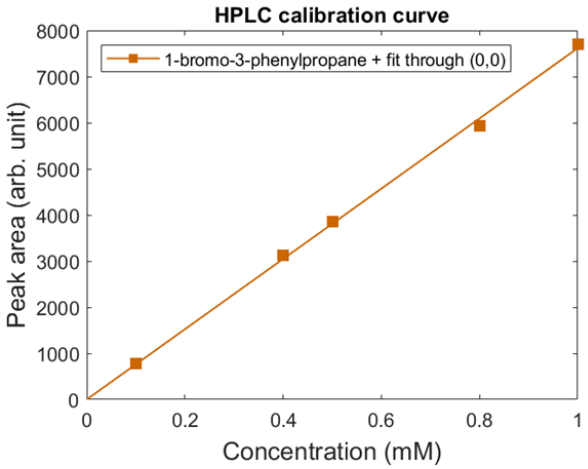

Fig. S7. High-performance liquid chromatography calibration curve for 1-bromo-3-phenylpropane, produced using a UV-Vis detector set at 210 nm.

Product characterization

Tert-butyl 2-(3-phenylpropyl)pyrrolidine-1-carboxylate

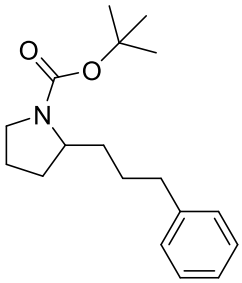

^{1}H NMR (400 MHz, $CDCl_3$): δ 7.25 – 7.15 (m, 2H), 7.10 (t, 3H), 4.25 (dd, 1H), 4.16 (dd, 1H), 4.12 – 3.99 (m, 1H), 3.53 – 3.23 (m, 1H), 2.64 – 2.52 (m, 2H), 2.36-2.09 (m, 3H), 1.99 – 1.83 (m, 2H), 1.81 – 1.70 (m, 2H), 1.33 (s, 9H). **^{13}C NMR (101 MHz, $CDCl_3$)**: δ 153.81, 140.94, 128.64, 126.01, 79.81, 64.15, 59.19, 46.32, 36.42, 32.09, 28.33, 24.32, 23.61.

Tert-butyl 2-(pent-4-en-1-yl)pyrrolidine-1-carboxylate

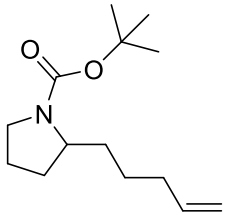

^{1}H NMR (400 MHz, $CDCl_3$): δ 5.73 (td, 1H), 4.95 (t, 1H), 4.28 – 4.22 (m, 1H), 4.20 – 3.97 (m, 1H), 3.56 – 3.24 (m, 2H), 2.12 – 1.98 (m, 3H), 2.00 – 1.74 (m, 4H), 1.68 (dd, 2H), 1.37 (s, 10H). **^{13}C NMR (101 MHz, $CDCl_3$)**: δ 153.80, 137.22, 115.40, 79.79, 59.18, 46.30, 30.92, 29.94, 28.32, 27.82, 24.28, 23.58.

Tert-butyl 2-(3-hydroxypropyl)pyrrolidine-1-carboxylate

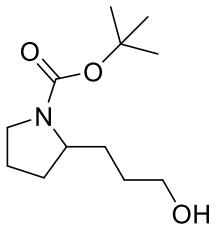

^{1}H NMR (400 MHz, $CDCl_3$): δ 4.27 – 4.11 (m, 1H), 3.62 (t, 2H), 3.52 – 3.26 (m, 2H), 2.57 (s, 1H) 2.22 – 2.04 (m, 4H), 1.98 – 1.72 (m, 3H), 1.37 (s, 10H). **^{13}C NMR (101 MHz, $CDCl_3$):** δ 154.50, 79.91, 62.02, 59.15, 46.59, 30.90, 29.90, 28.38, 28.28, 23.56.

Tert-butyl 2-cinnamylpyrrolidine-1-carboxylate

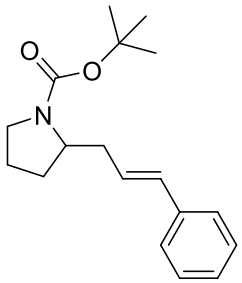

^{1}H NMR (400 MHz, $CDCl_3$): δ 7.30 (d, 2H), 7.20 (dt, 3H), 6.59 (d, 1H), 6.19 (dq, 1H), 4.79 – 4.61 (m, 2H), 3.56 – 3.25 (m, 1H), 2.26 – 1.99 (m, 2H), 2.00 – 1.68 (m, 3H), 1.34 (s, 10H). **^{13}C NMR (101 MHz, $CDCl_3$)**: δ 153.7, 134.62, 128.53, 128.11, 127.93, 126.56, 79.74, 65.35, 59.15, 46.29, 31.31, 28.23, 23.59.

Tert-butyl 2-(naphthalen-2-ylmethyl)pyrrolidine-1-carboxylate

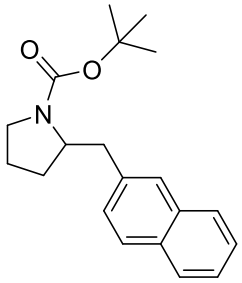

^{1}H NMR (400 MHz, $CDCl_3$): δ 7.91 (s, 2H), 7.74 (m, 2H), 7.47 – 7.34 (m, 3H), 7.32 – 7.12 (m, 1H), 4.77 – 4.56 (m, 2H), 3.59 – 3.21 (m, 1H), 2.27 – 2.01 (m, 2H), 1.99 – 1.64 (m, 3H), 1.27 (s, 10H). **^{13}C NMR (101 MHz, $CDCl_3$):** δ 154.44, 128.62, 127.99, 127.69, 127.59, 126.63, 126.35, 125.90, 65.43, 59.22, 46.58, 30.90, 29.93, 28.46, 28.22, 23.64.

Tert-butyl 2-cyclopentylpyrrolidine-1-carboxylate

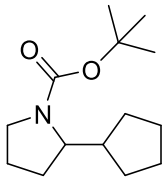

^{1}H NMR (400 MHz, $CDCl_3$): δ 5.12 (m, 2H), 4.15 (dd, 1H), 3.38 (ddd, 2H), 2.21 – 2.01 (m, 1H), 1.82 (dd, 5H), 1.57 (d, 6H), 1.37 (s, 9H). **13C NMR (101 MHz, $CDCl_3$):** δ 153.84, 59.26, 46.39, 32.67, 32.55, 30.84, 29.86, 28.46, 28.36, 24.21.

Tert-butyl 2-phenethylpyrrolidine-1-carboxylate

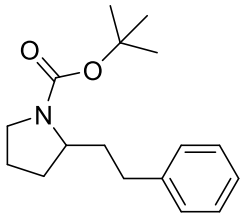

^{1}H NMR (400 MHz, $CDCl_3$): δ 7.34 – 7.08 (m, 5H), 5.84 (m, 2H), 4.22 (m, 2H), 3.54 – 3.22 (m, 1H), 2.24 – 2.00 (m, 2H), 1.93 – 1.68 (m, 2H), 1.53 – 1.46 (m, 2H) 1.25 (s, 9H). **^{13}C NMR (101 MHz, $CDCl_3$)**: δ 153.86, 141.52, 128.50, 128.41, 127.98, 79.74, 72.69, 59.15, 46.42, 30.87, 28.24, 24.19, 23.49.

Tert-butyl 2-(3-chloropropyl)pyrrolidine-1-carboxylate

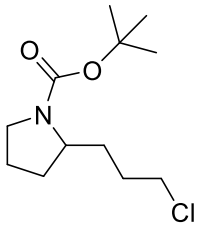

^{1}H NMR (400 MHz, $CDCl_3$): δ 4.30 – 4.01 (m, 1H), 3.58 – 3.49 (m, 2H), 3.51 – 3.16 (m, 2H), 2.23 – 2.08 (m, 1H), 2.08 – 1.99 (m, 5H), 1.97 – 1.72 (m, 1H), 1.34 (s, 10H). **^{13}C NMR (101 MHz, $CDCl_3$)**: δ 153.69, 79.82, 59.04, 46.28, 41.02, 31.49, 30.89, 29.76, 28.24, 23.56.

Tert-butyl 2-benzylpyrrolidine-1-carboxylate

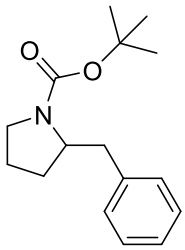

^{1}H NMR (400 MHz, $CDCl_3$): δ 7.30 – 7.21 (m, 5H), 5.08 (m, 2H), 4.31 (dd, 1H), 4.19 (dd, 1H), 3.54 – 3.21 (m, 1H), 2.22 – 2.03 (m, 2H), 1.98 – 1.68 (m, 2H), 1.24 (s, 9H). **^{13}C NMR (101 MHz, $CDCl_3$)**: δ 153.80, 135.81, 128.58, 128.29, 127.98, 66.60, 59.18, 46.33, 30.89, 29.89, 28.24, 24.30, 23.60.

Tert-butyl 2-(cyclohexylmethyl)pyrrolidine-1-carboxylate

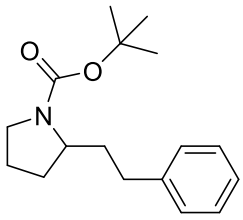

^{1}H NMR (400 MHz, $CDCl_3$): δ 4.21 (m, 1H), 3.86 (m, 2H), 3.55 – 3.17 (m, 2H), 2.28 – 1.99 (m, 1H), 1.99 – 1.73 (m, 2H), 1.62 (m, 6H), 1.37 (s, 9H), 1.13 (m, 4H), 0.98 – 0.68 (m, 2H). **^{13}C NMR (101 MHz, $CDCl_3$)**: δ 153.84, 79.78, 59.23, 46.28, 37.09, 30.94, 29.57, 28.30, 26.30, 25.59, 24.26, 23.57.

Tert-butyl 2-(2-(benzyloxy)ethyl)pyrrolidine-1-carboxylate

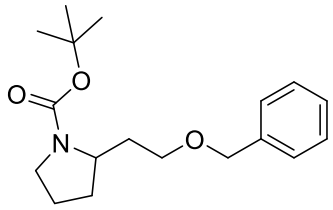

^{1}H NMR (400 MHz, $CDCl_3$): δ 7.28 – 7.18 (m, 5H), 4.85 (s, 1H), 4.34 – 4.09 (m, 2H), 3.64 – 3.53 (m, 2H), 3.50 – 3.16 (m, 3H), 2.22 – 2.05 (m, 2H), 1.97 – 1.69 (m, 2H), 1.32 (s, 10H). **^{13}C NMR (101 MHz, $CDCl_3$)**: δ 153.73, 137.82, 128.35, 127.67, 127.59, 79.74, 67.81, 59.04, 46.27, 36.37, 31.32, 29.89, 24.21, 23.51.

References

(1) Lin, Q.; Li, L.; Liang, S.; Liu, M.; Bi, J.; Wu, L. Efficient Synthesis of Monolayer Carbon Nitride 2D Nanosheet with Tunable Concentration and Enhanced Visible-Light Photocatalytic Activities. *Appl. Catal. B Environ.* **2015**, *163*, 135–142.

(2) Li, Y.; Jin, R.; Xing, Y.; Li, J.; Song, S.; Liu, X.; Li, M.; Jin, R. Macroscopic Foam-Like Holey Ultrathin g-C_3N_4 Nanosheets for Drastic Improvement of Visible-Light Photocatalytic Activity. *Adv. Energy Mater.* **2016**, *6* (24).

(3) Kresse, G.; Furthmüller, J. Efficient Iterative Schemes for Ab Initio Total-Energy Calculations Using a Plane-Wave Basis Set. *Phys. Rev. B* **1996**, *54* (16), 11169–11186.

(4) Kresse, G.; Hafner, J. Ab Initio Molecular Dynamics for Liquid Metals. *Phys. Rev. B* **1993**, *47* (1), 558–561.

(5) Blöchl, P. E. Projector Augmented-Wave Method. *Phys. Rev. B* **1994**, *50* (24), 17953–17979.

(6) Kresse, G.; Joubert, D. From Ultrasoft Pseudopotentials to the Projector Augmented-Wave Method. *Phys. Rev. B* **1999**, *59* (3), 1758–1775.

(7) Perdew, J. P.; Burke, K.; Ernzerhof, M. Generalized Gradient Approximation Made Simple. *Phys. Rev. Lett.* **1996**, *77* (18), 3865–3868.

(8) Heyd, J.; Scuseria, G. E.; Ernzerhof, M. Hybrid Functionals Based on a Screened Coulomb Potential. *J.*

Chem. Phys. **2003**, *118* (18), 8207–8215.

(9) Heyd, J.; Scuseria, G. E. Efficient Hybrid Density Functional Calculations in Solids: Assessment of the Heyd-Scuseria-Ernzerhof Screened Coulomb Hybrid Functional. *J. Chem. Phys.* **2004**, *121* (3), 1187–1192.

(10) Grimme, S.; Antony, J.; Ehrlich, S.; Krieg, H. A Consistent and Accurate Ab Initio Parametrization of Density Functional Dispersion Correction (DFT-D) for the 94 Elements H-Pu. *J. Chem. Phys.* **2010**, *132* (15).

(11) Grimme, S.; Ehrlich, S.; Goerigk, L. Effect of the Damping Function in Dispersion Corrected Density Functional Theory. *J. Comput. Chem.* **2011**, *32* (7), 1456–1465.

(12) Bardelang, D.; Camerel, F.; Ziessel, R.; Schmutz, M.; Hannon, M. J. New Organogelators Based on Cyclotriveratrylene Platforms Bearing 2-Dimethylacetal-5-Carbonylpyridine Fragments. *J. Mater. Chem.* **2008**, *18* (4), 489–494.

(13) Wang, Y.; Wang, X.; Antonietti, M. Polymeric Graphitic Carbon Nitride as a Heterogeneous Organocatalyst: From Photochemistry to Multipurpose Catalysis to Sustainable Chemistry. *Angew. Chem. Int. Ed.* **2012**, *51* (1), 68–89.

(14) Di Liberto, G.; Tosoni, S.; Pacchioni, G. Z-Scheme versus Type-II Junction in g-C_3N_4/TiO_2 and g-C_3N_4/$SrTiO_3$/TiO_2 Heterostructures. *Catal. Sci. Technol.* **2021**, *11* (10), 3589–3598.

(15) Nørskov, J. K.; Rossmeisl, J.; Logadottir, A.; Lindqvist, L.; Kitchin, J. R.; Bligaard, T.; Jónsson, H. Origin of the Overpotential for Oxygen Reduction at a Fuel-Cell Cathode. *J. Phys. Chem. B* **2004**, *108* (46), 17886–17892.

(16) Nørskov, J. K.; Bligaard, T.; Logadottir, A.; Kitchin, J. R.; Chen, J. G.; Pandelov, S.; Stimming, U. Trends in the Exchange Current for Hydrogen Evolution. *J. Electrochem. Soc.* **2005**, *152* (3), J23.

(17) Chan, K.; Tsai, C.; Hansen, H. A.; Nørskov, J. K. Molybdenum Sulfides and Selenides as Possible Electrocatalysts for CO_2 Reduction. *ChemCatChem* **2014**, *6* (7), 1899–1905.

(18) Calle-Vallejo, F.; Pohl, M. D.; Reinisch, D.; Loffreda, D.; Sautet, P.; Bandarenka, A. S. Why Conclusions from Platinum Model Surfaces Do Not Necessarily Lead to Enhanced Nanoparticle Catalysts for the Oxygen Reduction Reaction. *Chem. Sci.* **2017**, *8* (3), 2283–2289.

(19) Shang, R.; Steinmann, S. N.; Xu, B. Q.; Sautet, P. Mononuclear Fe in N-Doped Carbon: Computational

Elucidation of Active Sites for Electrochemical Oxygen Reduction and Oxygen Evolution Reactions. *Catal. Sci. Technol.* **2020**, *10* (4), 1006–1014.

(20) Van Dao, D.; Cipriano, L. A.; Di Liberto, G.; Nguyen, T. T. D.; Ki, S. W.; Son, H.; Kim, G. C.; Lee, K. H.; Yang, J. K.; Yu, Y. T.; Pacchioni, G.; Lee, I. H. Plasmonic Au Nanoclusters Dispersed in Nitrogen-Doped Graphene as a Robust Photocatalyst for Light-to-Hydrogen Conversion. *J. Mater. Chem. A* **2021**, *9* (40), 22810–22819.

(21) Di Liberto, G.; Cipriano, L. A.; Pacchioni, G. Role of Dihydride and Dihydrogen Complexes in Hydrogen Evolution Reaction on Single-Atom Catalysts. *J. Am. Chem. Soc.* **2021**, *143* (48), 20431–20441.

(22) *CRC Handbook of Chemistry and Physics*, 89th ed.; Lide, D. R., Ed.; CRC Press, Taylor and Francis Group: Boca Raton, FL, 2008.